

## Near-field distribution and propagation of scattering resonances in Vogel spiral arrays of dielectric nanopillars

F Intonti<sup>1,4</sup>, N Caselli<sup>1</sup>, N Lawrence<sup>2</sup>, J Trevino<sup>3</sup>, D S Wiersma<sup>1</sup>  
and L Dal Negro<sup>2,3,4</sup>

<sup>1</sup> LENS and Department of Physics, University of Florence, I-50019 Sesto Fiorentino, Italy

<sup>2</sup> Department of Electrical and Computer Engineering and Photonics Center, Boston University, Boston, MA, USA

<sup>3</sup> Division of Materials Science and Engineering, Boston University, Brookline, MA, USA

E-mail: [intonti@lens.unifi.it](mailto:intonti@lens.unifi.it) and [dalnegro@bu.edu](mailto:dalnegro@bu.edu)

*New Journal of Physics* **15** (2013) 085023 (12pp)

Received 27 February 2013

Published 22 August 2013

Online at <http://www.njp.org/>

doi:10.1088/1367-2630/15/8/085023


**Abstract.** In this work, we employ scanning near-field optical microscopy, full-vector finite difference time domain numerical simulations and fractional Fourier transformation to investigate the near-field and propagation behavior of the electromagnetic energy scattered at  $1.56\ \mu\text{m}$  by dielectric arrays of silicon nitride nanopillars with chiral  $\alpha_1$ -Vogel spiral geometry. In particular, we experimentally study the spatial evolution of scattered radiation and demonstrate near-field coupling between adjacent nanopillars along the parastichies arms. Moreover, by measuring the spatial distribution of the scattered radiation at different heights from the array plane, we demonstrate a characteristic rotation of the scattered field pattern consistent with net transfer of orbital angular momentum in the Fresnel zone, within a few micrometers from the plane of the array. Our experimental results agree with the simulations we performed and may be of interest to nanophotonics applications.

<sup>4</sup> Authors to whom any correspondence should be addressed.



Content from this work may be used under the terms of the [Creative Commons Attribution 3.0 licence](https://creativecommons.org/licenses/by/3.0/).

Any further distribution of this work must maintain attribution to the author(s) and the title of the work, journal citation and DOI.

 Online supplementary data available from [stacks.iop.org/NJP/15/085023/mmedia](http://stacks.iop.org/NJP/15/085023/mmedia)

## Contents

<b>1. Introduction</b>	<b>2</b>
<b>2. Experimental methods</b>	<b>3</b>
<b>3. Results and discussion</b>	<b>4</b>
<b>4. Conclusions</b>	<b>11</b>
<b>Acknowledgments</b>	<b>11</b>
<b>References</b>	<b>11</b>

## 1. Introduction

The generation of complex light beams carrying orbital angular momentum (OAM) to the far field using optical nanostructures is attracting considerable attention in singular optics for potential applications to super-resolution imaging, optical communications, quantum optics and information security. Most research efforts have so far focused on the engineering of near-field coupling in metallic nanostructures with tailored optical resonances [1] or array geometries [2–4] in relation to the generation of optical vortices and structured light with well-defined OAM in the far field. Among the different approaches investigated so far, Vogel spiral arrays of Au nano-cylinders and dielectric nanopillars are interesting owing to their largely tuneable chiral and geometrical properties, described by correlation functions in between disordered random systems and quasi-periodic crystals [5].

Vogel spiral arrays are a broad class of deterministic aperiodic structures that have been investigated for centuries by mathematicians, botanists and theoretical biologists [6] in relation to the outstanding geometrical problems of *phyllotaxis* [7–10], which is concerned with the understanding of the arrangement of leaves, bracts and florets on plant stems. Vogel spirals exhibit circularly symmetric scattering rings in Fourier space entirely controlled by simple generation rules that induce structural correlations in between amorphous and random systems [5].

Vogel spiral arrays of  $n$  particles are defined in polar coordinates  $(r, \theta)$  by the simple relations [6, 11–13]:

$$r_n = a_0 \sqrt{n}, \quad (1)$$

$$\theta_n = n\xi, \quad (2)$$

where  $n = 1, 2, \dots$  is an integer index,  $a_0$  is a constant scaling factor and  $\xi$  is the divergence angle, which is an irrational number. This angle gives the constant aperture between successive particles in the spiral array. The most commonly studied Vogel spiral is known as the golden angle (GA) spiral, generated with a divergence angle equal to the GA  $\xi = \alpha$  ( $\sim 137.51^\circ$ ). The GA  $\alpha$  is related to the famous Fibonacci golden number  $\varphi = (1 + \sqrt{5})/2 \approx 1.618$  by the relation  $\alpha = 360/\varphi^2$ . Rational approximations to the GA can be obtained by the formula  $\alpha = 360 \times (1 + p/q)^{-1}$  where  $p$  and  $q < p$  are consecutive Fibonacci numbers.

Since  $\alpha$  is an irrational number, the GA spiral lacks both translational and rotational symmetry. Accordingly, its spatial Fourier spectrum does not exhibit well-defined Bragg peaks,

as for standard photonic crystals and quasi-crystals, but rather features a diffuse circular ring whose position varies with wavelength, particle spacing and array geometry, as determined by the angle  $\xi$ . The structure of a GA spiral can be decomposed into clockwise (CW) and counterclockwise (CCW) families of out-spiraling arms of particles, known as *parastichies*, which stretch out from the center of the arrays. The number of spiral arms in the parastichies is given by consecutive Fibonacci numbers.

Previous studies have mostly focused on three types of aperiodic spirals, including the GA-spiral and two other structures obtained by the following choices of divergence angles:  $137.3^\circ$  (i.e.  $\alpha_1$ -spiral) and  $137.6^\circ$  (i.e.  $\alpha_2$ -spiral or  $\beta_4$ -spiral) [6–8, 13]. The  $\alpha_1$ - and  $\beta_4$ -spirals are called ‘nearly golden spirals’, their parastichies are considerably fewer, and they exhibit a more disordered spatial structure compared to the GA-spiral resulting in far richer spectra of localized optical modes. Vogel spiral arrays of resonant Au nanoparticles have been shown to give rise to polarization-insensitive light diffraction across a broad spectral range and to support a broad spectrum of distinctive scattering resonances carrying OAM [2], which have been exploited in a number of optical device structures [2–4, 14, 15].

Controlled generation and manipulation of OAM states with large values of azimuthal numbers have been recently analytically modeled [3] and demonstrated experimentally using various types of Vogel arrays of metal nanoparticles [4], providing opportunities for the generation of complex OAM spectra using planar nanoparticle arrays. More recently, the interaction of optical beams with two-dimensional nanostructures of designed chirality became a topic of great interest from both a fundamental and a technological standpoint due to the possibility to directly manipulate chiral effects in light–matter coupling by near-field engineering [16].

In this study, using scanning near-field optical microscopy combined with light scattering simulations based on full-vector finite difference time domain (FDTD) and efficient fractional Fourier transform (FRFT), we investigate the spatial evolution of characteristic scattering resonances in arrays of dielectric nanopillars with chiral  $\alpha_1$  Vogel spiral geometry. In particular, different from most of the previous works that focused on metallic nanostructures, here we consider optically transparent, high-refractive index silicon nitride nanopillar structures and their near-field coupling behavior, and we experimentally show net transfer of OAM by wave diffraction in spiral geometry within few micrometers from the plane of the array. We specifically focused our study on the optical behavior of the  $\alpha_1$  Vogel spiral because it is an example of a deterministic chiral structure with an almost constant pair-correlation function, similarly to the case of random gases [5]. As a result, the  $\alpha_1$  Vogel spiral features a characteristic interplay between structural disorder and the well-defined CCW chirality that could potentially lead to novel wave diffraction and self-imaging phenomena, as addressed in this paper for the first time.

## 2. Experimental methods

The spiral nanopillar array fabrication process begins by depositing a 650 nm thick silicon rich nitride (SRN) layer by radio frequency magnetron sputtering onto a silicon dioxide ( $\text{SiO}_2$ ) substrate [17]. Electron beam lithography is used to define the spiral geometry in a poly(methyl methacrylate) resist [18]. A 40 nm thick chrome (Cr) mask layer was deposited via electron beam evaporation, followed by a subsequent lift-off process in heated acetone. Reactive ion etching is used to transfer the pattern to the SRN, resulting in 350 nm tall SRN pillars, and

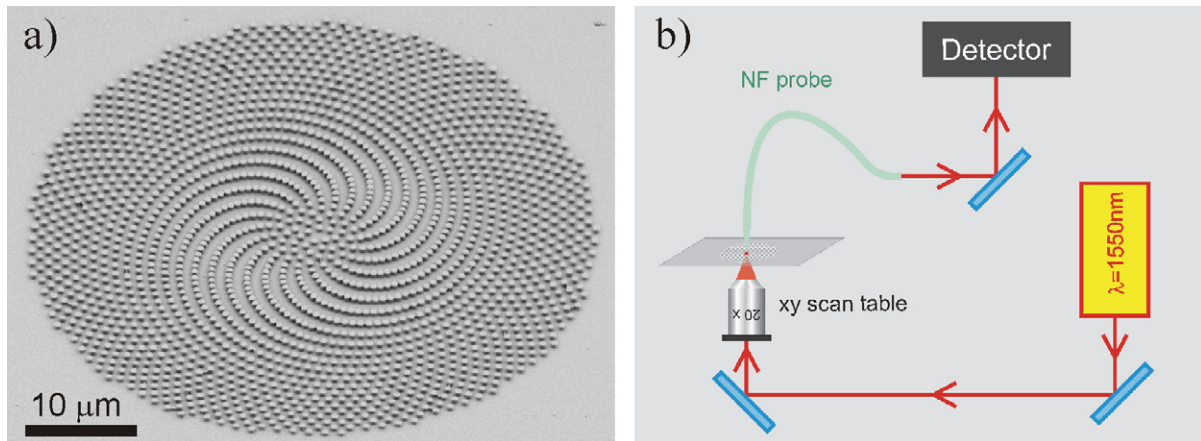


**Figure 1.** (a) SEM micrograph of  $\alpha_1$  spiral nanopillar array with array diameter of  $50\ \mu\text{m}$ , pillar diameter of  $520\ \text{nm}$  and pillar height of  $350\ \text{nm}$ . (b) SNOM configuration with uncoated near-field probes in transmission geometry. The light source is a diode laser emitting at  $\lambda = 1556\ \text{nm}$ .

leaving a  $300\ \text{nm}$  SRN film beneath. The Cr mask layer is then removed by wet chemical etchant. The  $\alpha_1$ -spiral array diameter is  $50\ \mu\text{m}$ , consisting of 1965 pillars each with individual pillar diameter of  $520\ \text{nm}$ . A scaling factor ( $a_0$ ) of  $564\ \text{nm}$  was used, resulting in an average nearest-neighbor center to center spacing of  $900\ \text{nm}$ . This value is calculated by finding the distance from a particle to every other particle in the array, the minimum of those values gives the distance to the nearest neighbor. By repeating this for each particle in the array and averaging the results, the average nearest-neighbor separation is then obtained. A scanning electron microscopy (SEM) micrograph of the fabricated  $\alpha_1$ -spiral is shown in figure 1(a) showing that the structure is characterized by 21 parastichies arms.

Optical field measurements were performed with a commercial scanning near-field optical microscope (SNOM) (TwinSNOM, Omicron) with shear-force feedback equipped with uncoated near-field probes in transmission geometry. The light from a diode laser ( $\lambda = 1556\ \text{nm}$ ) is focused on the back side of the sample with a  $20\times$  objective ( $\text{NA} = 0.4$ ) and the transmitted light is collected through the near-field probe, as shown in figure 1(b). We performed experiments with two different laser spot dimensions. The first configuration, used for near-field measurements, maintains an optimal focus on the sample surface, resulting in a laser spot with a diameter of few microns. In this configuration, approximately ten pillars are illuminated at a time. A second configuration used to take far-field measurements, utilizes a defocused laser beam to illuminate the entire spiral pillar array at once. The latter configuration contributes to the enhancement of interference effects in the far field since each pillar acts as a scattering center and collective effects are more pronounced.

### 3. Results and discussion

Using the SNOM setup discussed above, we have investigated experimentally the spatial distribution of the optical intensity scattered by the fabricated  $\alpha_1$  spiral at  $1.56\ \mu\text{m}$ . Figure 2(a) displays the overall electric field intensity distribution of the  $\alpha_1$  spiral with  $50\ \mu\text{m}$  diameter

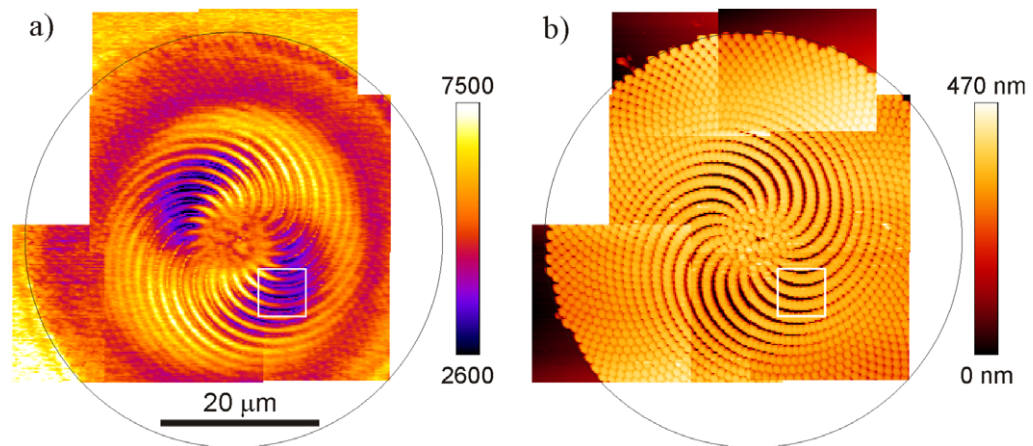


**Figure 2.** (a) Near-field optical map of an  $\alpha_1$  spiral with  $50 \mu\text{m}$  diameter excited at  $\lambda = 1556 \text{ nm}$ , assembled by connecting multiple near-field scans collected on different  $20 \times 20 \mu\text{m}^2$  areas. Outer circle defines the position of outer array edge. (b) Topography map of  $\alpha_1$  spiral acquired simultaneously with the optical data shown in (a).

obtained by connecting different near-field scans collected on  $20 \times 20 \mu\text{m}^2$  areas. From this image, we extract a typical spatial resolution of  $250 \text{ nm}$ . Figure 2(b) shows the spiral geometry extracted from the reassembled topography image, which is acquired simultaneously with optical data. By comparing the reassembled optical image and the topography, near-field coupling is observed unambiguously between nanopillars along the parastichies arms.

In order to accurately investigate where the transmitted optical intensity is concentrated, figure 3 is magnified, both for the optical image and for the topography, the  $6 \times 6 \mu\text{m}^2$  region highlighted by the white squares in figure 2. A direct comparison of the optical distribution with the topographic image reveals that the transmitted signal originates from the top of the pillars forming parastichies arms and from the substrate region between two parastichies arms, highlighted by the corresponding white arrows in figure 3. However, the highest field intensities are recorded near the top of the pillars forming the parastichies arms.

To better understand the near-field coupling effects within the parastichies, we carried out three-dimensional (3D) FDTD simulations, using a commercial software package (Lumerical Solutions)<sup>5</sup>. The exact 3D geometry of the device was considered in the simulation. However, owing to computational memory limitations, the spiral array was limited to the first 500 pillars. The device is placed on a  $\text{SiO}_2$  substrate and excited from the bottom (through substrate) by a plane wave at  $1550 \text{ nm}$  to match the experimental conditions as closely as possible. Perfectly matched layer boundary conditions are used to terminate the simulation domain. To reduce the presence of the pump beam in the far-field plots, the source contribution was subtracted from the simulation immediately above the array, leaving only the contribution of the scattered light.

Field monitors were placed in the device to measure the electric field intensity at the top and bottom of the nanopillars, as well as at various planes above the array in order to study the evolution of the field structure as it propagates in space away from the pillars plane. The results of the numerical simulations are summarized in figure 4. Figure 4(a)

<sup>5</sup> Lumerical Solutions, Inc. ([www.lumerical.com/tcad-products/fdtd](http://www.lumerical.com/tcad-products/fdtd)).



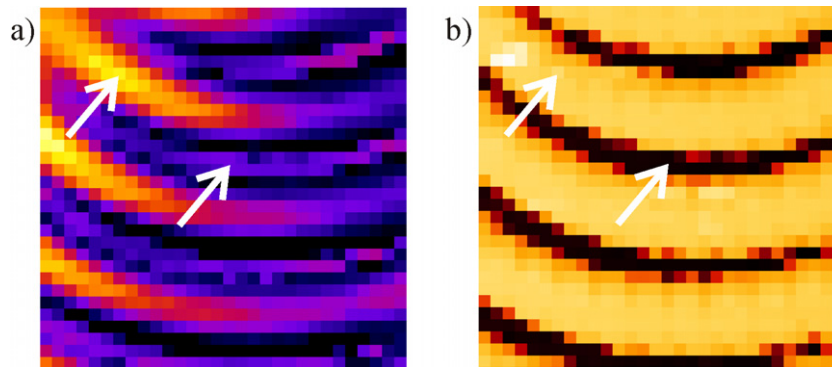


**Figure 3.** Magnified image of the (a) optical near field and the (b) topography of the  $6 \times 6 \mu\text{m}^2$  region highlighted by the white squares in figures 2(a) and (b), respectively. The white arrows are placed at same positions in both images and help to identify a parastichies arm and its neighboring substrate region.

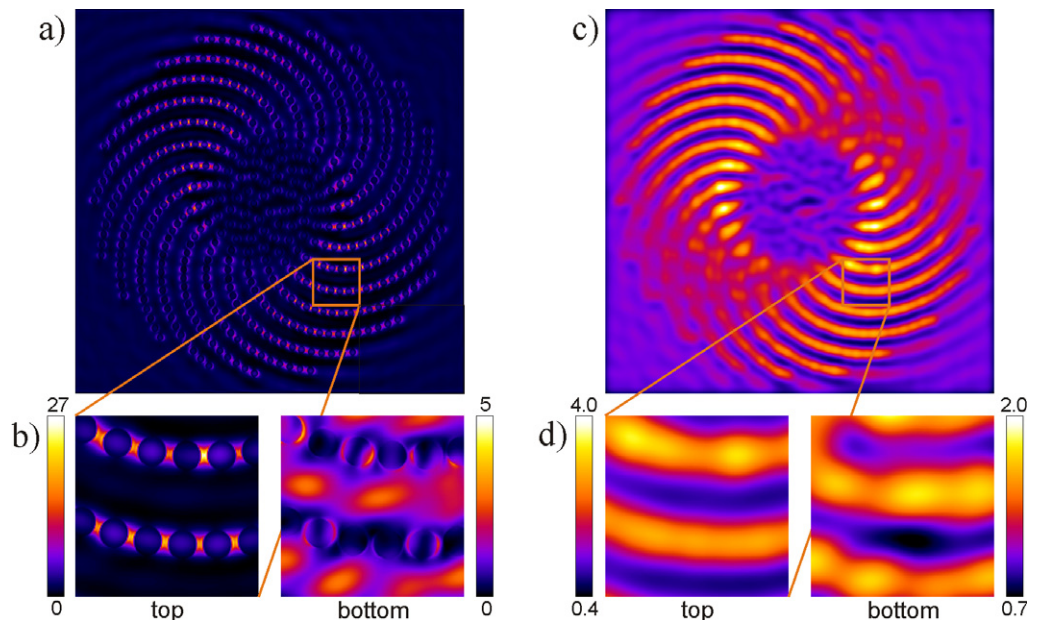


**Figure 4.** (a) Simulated (3D FDTD) electric field intensity distribution of the first 500 nanopillars of an  $\alpha_1$  spiral, excited with a plane wave at  $\lambda = 1550 \text{ nm}$ . The electric field is plotted at the top surface of the nanopillars. (b) Magnified plot measuring  $3.6 \times 3.6 \mu\text{m}^2$  of the region highlighted by orange box in (a). The electric field distribution is plotted in the top plane (left) and bottom plane (right) of the nanopillars. The same field distributions of (a) and (b) are convolved with a Gaussian, characterized by a FWHM of 250 nm, and are plotted in (c) and (d), respectively.

shows the distribution of the electric field intensity sampled in the top plane of the pillars. Figure 4(b) displays a magnified area ( $3.6 \times 3.6 \mu\text{m}^2$ ) encircled by the orange box in figure 4(a) and approximately corresponding to the central part of the region investigated in figure 3.

Both the electric field intensity at the top detector and the bottom detector are plotted in figure 4(b). As observed experimentally in the SNOM measurements, the field intensity measured by the top detector is concentrated between two subsequent pillars forming the parastichies, while in the bottom detector the signal mostly originates from the substrate plane. In figures 4(c) and (d), we reported the same field distributions of figures 4(a) and (b) convolved with a Gaussian function, characterized by a full-width at half-maximum (FWHM) of 250 nm, in order to take into account the finite spatial resolution of our experimental setup. It is evident that the main effect of the Gaussian convolution is to blur the images. After convolution, it is no longer possible to distinguish by analyzing the top detector that the signal is localized in the regions between two adjacent pillars. Nevertheless, it is still clear that the optical energy flows along the parastichies. In contrast, when analyzing the data collected by the bottom detector, we observe that the electric field intensity has a maximum on the substrate. It is also remarkable that, as a consequence of the Gaussian convolution, the electric field intensity maxima drop from 27 to 4 in the top detector and from 5 to 2 in the bottom detector, respectively. It follows that the comparison between the experimental and the calculated electric field intensity distributions is quantitatively very good, as it is clear by comparing figure 3(a) with figure 4(d). Here, the signal collected by the near-field probe on the parastichies should be associated with the top detector of the simulation, and the signal collected when the near-field probe reaches the substrate should be compared with the bottom detector.

In the following, we address the wave diffraction properties of the sample by studying the intensity distribution of the field scattered by the SRN  $\alpha_1$  spiral at different heights from the pillars array. Figures 5(a) and (b) show the numerical FDTD calculations of the electric field intensity calculated with a field monitor placed 1 and 4  $\mu\text{m}$  above the  $\alpha_1$  spiral, respectively. In figures 5(c) and (d), we plot the experimentally measured scattered fields, collected within a  $30 \times 30 \mu\text{m}^2$  region, and probed at a constant height of approximately 2 and 6  $\mu\text{m}$  away from the sample surface, respectively. We can observe that at a distance of 1–2  $\mu\text{m}$  from the sample surface, the spatial distribution of the electric field is characterized by the 21 curved arms associated with the parastichies that follow a CCW orientation, as observed in both measurements and calculations. However, by increasing the distance from the surface, the 21 curved arms are still unambiguously discernable, but now appear with a CW orientation, demonstrating a remarkable inversion in the optical intensity pattern along its propagation direction in free space. This interesting inversion of the propagating field pattern is observed both in the numerical calculations and the experimental data. However, minor differences between the experiment and calculations results both from the uncertainty in the experimental determination of the height of the measuring plane and from the fact that the uncoated probe collects signal at slightly different heights. In fact, the SNOM setup used lacks calibration for determining the sample-to-probe distance when the probe is not in feedback.

To further explore the spatial evolution of the scattered field pattern as it propagates away from the pillars array, we have carried out additional FDTD calculations as a function of the propagation distance and created a video combining all the frames, which is available as supplementary material (available from [stacks.iop.org/NJP/15/085023/mmedia](http://stacks.iop.org/NJP/15/085023/mmedia)). The supplementary video illustrates the evolution of the scattered field intensity as it propagates from the top plane of the pillars up to 8  $\mu\text{m}$  above the array plane in approximately 0.1  $\mu\text{m}$  vertical steps. Through the entire progression of vertical planes, we can observe unambiguously that the overall field pattern continuously passes from a CCW rotation to a CW rotation. The parastichy field components begin with a CCW orientation, exactly following in the near-field

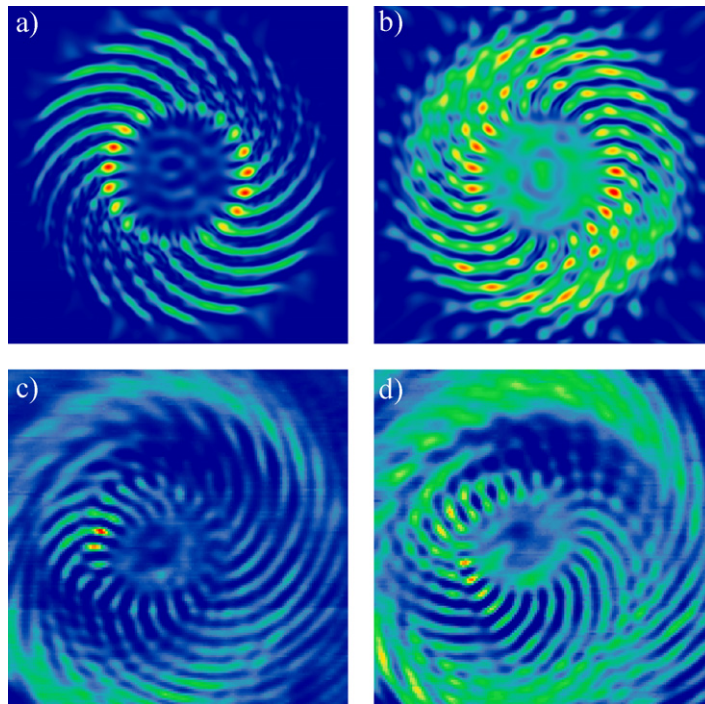


**Figure 5.** Numerical 3D FDTD calculations of the electric field intensity calculated with detectors placed at (a)  $1\ \mu\text{m}$  and (b)  $4\ \mu\text{m}$  above the  $\alpha_1$  spiral. SNOM scans collected at a constant height modulus approximately (c)  $2\ \mu\text{m}$  and (d)  $6\ \mu\text{m}$  away from the sample surface, respectively. All the maps cover an area of  $30 \times 30\ \mu\text{m}^2$ .

zone the geometry of the arms. However, as the plane of observation reaches approximately  $3\ \mu\text{m}$ , the parastichies field pattern evolves into a mixture of both CCW and CW arms, slowly transitioning into purely CW arms when propagating in between the  $4$  and the  $8\ \mu\text{m}$  observation planes.

The distinct rotation of the scattered field intensity highlights the very rich dynamics of interacting scattered wavelets that transfer net orbital momentum to the overall radiation field in the intermediate Fresnel zone. To the best of our knowledge, the data in figure 5 provide the first evidence of net OAM transfer occurring within few micrometers from the object in Vogel spiral arrays of dielectric nanopillars. In fact, while previous studies have focused on the rich spectrum of azimuthal OAM values transferred to the far-field radiation zone by Vogel spirals [3, 4, 19], the complex wave diffraction effects that develop in the intermediate Fresnel zone remain to be explored.

In order to investigate the free propagation of the scattered field intensity over a larger range of distances, we have resorted to the method of fractional Fourier transformation. This approach provides an equivalent formulation of the paraxial wave propagation and Fresnel scalar diffraction theory [20], and considers light propagation as a process of continual fractional transformation of increasing order. However, this approach neglects materials dispersion and the spiral array is modeled by circular apertures within the scalar approximation. The FRFT is a well-known generalization in fractional calculus of the familiar Fourier transform operation,



and it has successfully been applied to the study of quadratic phase systems, imaging systems and diffraction problems, in general [20–23].

Given a function  $f(u)$ , under the same conditions in which the standard Fourier transform exists, we can define the  $a$ th order FRFT  $f_a(u)$  with  $a$  being a *real number* in several equivalent ways [20, 24]. The most direct definition of the FRFT is given in terms of the linear integral transform:

$$f_a(u) \equiv \int_{-\infty}^{\infty} K_a(u, u') f(u') du' \quad (3)$$

with kernel defined by [20]

$$\begin{aligned} K_a(u, u') &\equiv A_\alpha \exp[i\pi(u^2 \cot \alpha - 2uu' \csc \alpha + u'^2 \cot \alpha)], \\ A_\alpha &\equiv \sqrt{1 - i \cot \alpha}, \\ \alpha &\equiv \frac{a\pi}{2}, \end{aligned} \quad (4)$$

for  $a \neq 2n$  and  $K_a(u, u') = \delta(u - u')$  when  $a = 4n$ , and  $K_a(u, u') = \delta(u + u')$  when  $a = 4n \pm 2$ , with  $n$  an integer. The  $a$ th order fractional transform defined above is sometimes called the  $\alpha$ th order transform and it coincides with the standard (i.e. integer) Fourier transform for  $a = 1$  or  $\pi/2$ . More information on alternative definitions, generalizations and the many properties of FRFTs can be found in [20, 24]. The FRFT of a function can be thought of as the Fourier transform to the  $n$ th power, where  $n$  need not be an integer. Moreover, being a particular type of *linear canonical transformation*, the FRFT maps a function to any intermediate domain between time and frequency and can be interpreted as a *rotation in the time–frequency domain* [20].

In optics, the main advantage of the FRFT method compared with numerical FDTD simulation relies on its superior computational efficiency, which enables a more detailed investigation of the qualitative behavior of the intensity propagation over an extended propagation range. In this paper, we computed the two-dimensional FRFT according to [25] (<http://nalag.cs.kuleuven.be/research/software/FRFT/frft22d.m>) and studied the propagation of the diffracted field up to  $50 \mu\text{m}$  above the spiral plane. We additionally prepared a high-resolution movie that illustrates the free-field propagation of the intensity scattered by the Vogel spiral, and we have included this as supplementary material (available from [stacks.iop.org/NJP/15/085023/mmedia](http://stacks.iop.org/NJP/15/085023/mmedia)). In figure 6, we show few representative movie frames that display the FRFT-calculated intensity at different distances from the spiral plane, as specified in the caption. We can clearly appreciate in figures 6(c) and (g) the cases in which the diffracted field patterns are rotated with respect to the geometry of the parastichies arms, as previously discussed in relation to figure 5. However, the emergence of this rotation phenomenon from the FRFT scalar field simulations demonstrates its very robust and general nature, which follows from the coherent interactions of (singly) diffracted wavelets in the central and more disordered area of the spiral array, as evident in figures 6(c), (f) and (g). In particular, we can appreciate from the field evolution in the near-field region (figure 6(c)) that the central area of the spiral couples radiation into directions that are orthogonal to the surrounding parastichies arms. These secondary lines of scattered radiation spatially define a complementary set of parastichies arms that are responsible for the inversion of the intensity pattern at short distances from the object plane. As propagation unfolds, the diffracted wavelets coherently reinforce each other along distinctively rotating ring-like structures observed in figures 6(f) and (g), which gradually transition at larger distances into the characteristic circularly

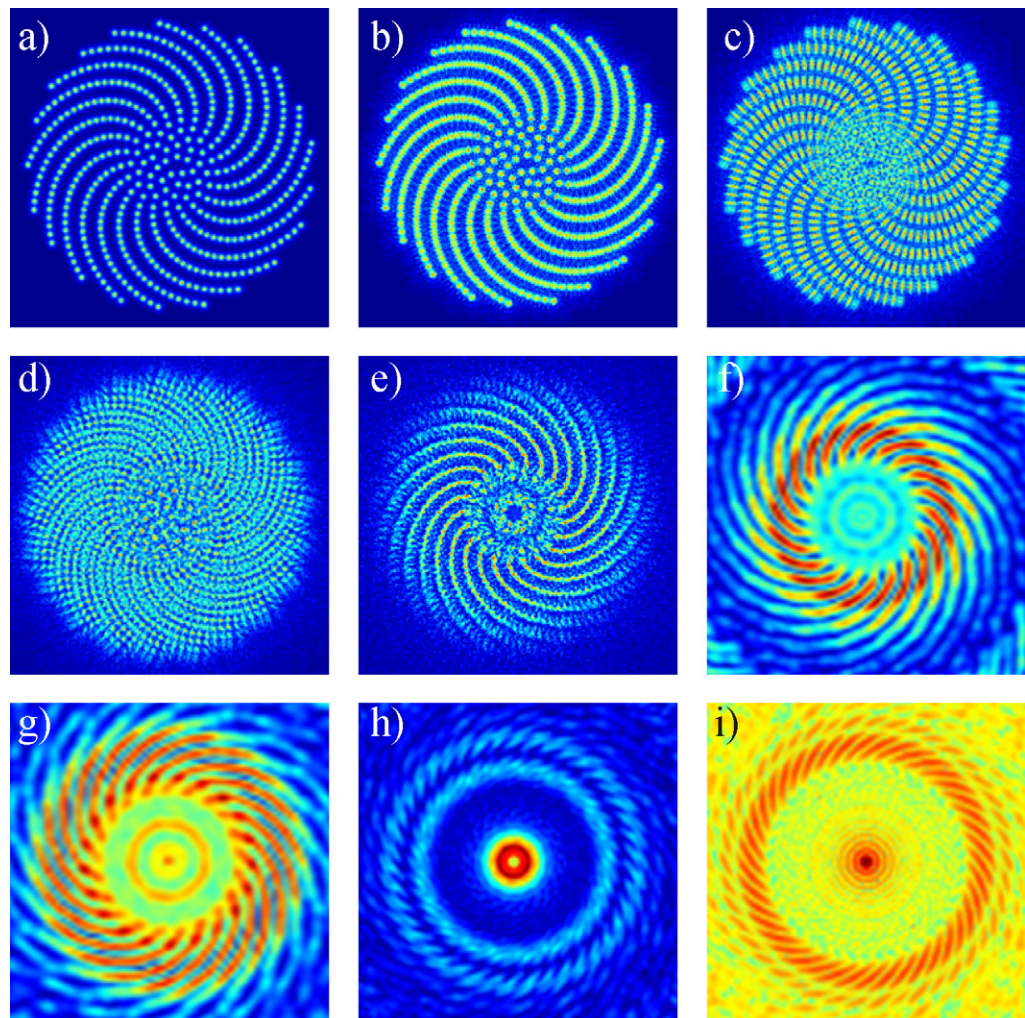


**Figure 6.** Magnitude of electric field propagated to different planes calculated using the FRFT method. Propagation distance for panels (a)–(h) are 0.01, 0.043, 0.078, 0.107, 0.457, 1.95, 2.68 and 6.5  $\mu\text{m}$ , respectively. Panel (i) shows the far-field in  $\log_{10}$  scale.

symmetric far-field patterns of Vogel spirals (figure 6(i)) [2, 5]. However, depending on the propagation distance, we have observed (see accompanying movie) a characteristic oscillation between the formation of ring-like structures and the inversion of the field intensity patterns compared with the image of the spiral geometry. We believe that this effect unveils a distinctive self-imaging property of Vogel spirals, which is particularly evident in figures 6(e) and (g). We recall that full image reconstruction will happen at a distance  $L$  from a coherently illuminated array with discrete spatial frequencies located in reciprocal space at rings of radii  $\rho^2 = 1/\lambda^2 - (m/L)^2$ , where  $m$  is an integer such that  $0 \leq m \leq L/\lambda$  [26]. Self-imaging effects have been vastly investigated in the context of periodic structures (e.g. the Talbot effect) as well as in quasi-periodic Penrose arrays, where it has been recently shown that they can focus light into sub-wavelength spots in the far field without contributions from evanescent fields [27–29]. However, to the best of our knowledge, self-imaging effects in aperiodic media with isotropic

Fourier space that lacks diffraction peaks have never been demonstrated before, and will be the subject of a more extended follow up paper.

The results in figure 6 and the corresponding movie indicate that the unique propagation behavior of diffracted waves from the  $\alpha_1$  spiral results from the coherent interplay of two well-separated spatial regions of very dissimilar structural order: (i) on one side the disordered central region of the spiral that diffracts wavelets in any direction, and (ii) the surrounding region with the well-defined chirality of the parastichies arms on the other side. In this region, the radiated optical power from each excited particle defines an inverted set of orthogonal parastichies arms and ‘inverts’ the spatial pattern of the self-images of the array. We believe that the unique interplay between aperiodic order and chiral structures such as the investigated  $\alpha_1$  spiral can provide novel opportunities for the manipulation of sub-wavelength optical fields and disclose richer scenarios for the engineering of focusing and self-imaging phenomena in nanophotonics.

#### 4. Conclusions

In this work, by using scanning near-field optical microscopy, FDTD numerical simulations and the FRFT method, we have investigated the near-field coupling behavior and the propagation of electromagnetic energy distribution of scattered radiation from silicon nitride-based arrays of nanopillars with  $\alpha_1$  spiral geometry. In particular, we studied the spatial distribution of scattered radiation at  $1.56 \mu\text{m}$ , and found excellent agreement between numerical simulations and SNOM data demonstrating near-field coupling of dielectric pillars along the parastichies arms. Moreover, by measuring and computing the spatial structure of the scattered field at different heights from the array plane, we have demonstrated experimentally net orbital momentum transfer to the radiation field occurring within few micrometers from the array plane, in agreement with FRFT diffraction calculations in the paraxial regime. We believe that the unique features of structurally disordered and chiral Vogel spirals provide interesting new opportunities for a number of engineering applications in singular optics, secure communication, imaging and optical sensing.

#### Acknowledgments

This work was supported by the AFOSR programs under Awards FA9550-10-1-0019 and FA9550-13-1-0011, by the NSF Career Award number ECCS-0846651 and by the European Network of Excellence on Nanophotonics for energy efficiency and the Advanced ERC grant Photbots.

#### References

- [1] Yu N, Genevet P, Kats M A, Aieta F, Tetienne J-P, Capasso F and Gaburro Z 2011 Light propagation with phase discontinuities: generalized laws of reflection and refraction *Science* **334** 333–7
- [2] Trevino J, Cao H and Dal Negro L 2010 Circularly symmetric light scattering from nanoplasmonic spirals *Nano Lett.* **11** 2008–16
- [3] Dal Negro L, Lawrence N and Trevino J 2012 Analytical light scattering and orbital angular momentum spectra of arbitrary Vogel spirals *Opt. Express* **20** 18209–23
- [4] Lawrence N, Trevino J and Dal Negro L 2012 Control of optical orbital angular momentum by Vogel spiral arrays of metallic nanoparticles *Opt. Lett.* **37** 5076

- [5] Trevino J, Liew S F, Noh H, Cao H and Dal Negro L 2012 Geometrical structure, multifractal spectra and localized optical modes of aperiodic Vogel spirals *Opt. Express* **20** 3015–33
- [6] Vogel H 1979 A better way to construct the sunflower head *Math. Biosci.* **44** 179
- [7] Ball P 2009 *Shapes. Nature's Patterns: A Tapestry in Three Parts* (New York: Oxford University Press)
- [8] Jean R V 1995 *Phyllotaxis: A Systematic Study in Plant Morphogenesis* (Cambridge: Cambridge University Press)
- [9] Mitchison G J 1977 Phyllotaxis and the Fibonacci series *Science* **196** 270–5
- [10] Thompson D A W 1992 *On Growth and Form* (New York: Dover)
- [11] Pollard M E and Parker G J 2009 Low-contrast bandgaps of a planar parabolic spiral lattice *Opt. Lett.* **34** 2805–7
- [12] Naylor M 2002 Golden,  $\sqrt{2}$ , and  $\pi$  flowers: a spiral story *Math. Mag.* **75** 163–72
- [13] Adam J A 2009 *A Mathematical Nature Walk* (Princeton, NJ: Princeton University Press)
- [14] Trevino J, Forestiere C, Di Martino G, Yerci S, Priolo F and Dal Negro L 2012 Plasmonic–photonic arrays with aperiodic spiral order for ultra-thin film solar cells *Opt. Express* **20** A418–30
- [15] Capretti A, Walsh G F, Minissale S, Trevino J, Forestiere C, Miano G and Dal Negro L 2012 Multipolar second harmonic generation from planar arrays of Au nanoparticles *Opt. Express* **20** 15797–806
- [16] Gorodetski Y, Drezet A, Genet C and Ebbesen T W 2013 Generating far-field orbital angular momenta from near-field optical chirality *Phys. Rev. Lett.* **110** 203906
- [17] Gopinath A, Boriskina S V, Yerci S, Li R and Dal Negro L 2010 Enhancement of the 1.55  $\mu\text{m}$  Erbium emission from quasiperiodic plasmonic arrays *Appl. Phys. Lett.* **96** 071113
- [18] Lawrence N, Trevino J and Dal Negro L 2012 Aperiodic arrays of active nanopillars for radiation engineering *J. Appl. Phys.* **111** 113101
- [19] Liew S F, Noh H, Trevino J, Dal Negro L and Cao H 2011 Localized photonic bandedge modes and orbital angular momenta of light in a golden-angle spiral *Opt. Express* **19** 23631–42
- [20] Ozaktas H M, Zalevsky Z and Alper Kutay M 2001 *The Fractional Fourier Transform with Applications in Optics and Signal Processing* (Chichester: Wiley)
- [21] Mendlovic D and Ozaktas H M 1993 Fractional Fourier transforms and their optical implementation: I *J. Opt. Soc. Am. A* **10** 1875
- [22] Ozaktas H M and Mendlovic D 1993 Fractional Fourier transforms and their optical implementation: II *J. Opt. Soc. Am. A* **10** 2522
- [23] West B J, Bologna M and Grigolini P 2003 *Physics of Fractal Operators* (New York: Springer)
- [24] Narayanan V A and Prabhu K M M 2003 The fractional Fourier transform: theory, implementation and error analysis *Microprocess. Microsyst.* **27** 511
- [25] Bultheel A and Martínez-Sulbaran H 2004 Computation of the fractional Fourier transform *Appl. Comput. Harmon. Anal.* **16** 182
- [26] Montgomery W D 1967 Self-imaging objects of infinite apertures *J. Opt. Soc. Am.* **57** 772
- [27] Huang F M, Chen Y, Javier Garcia de Abajo F and Zheludev N I 2007 Optical super-resolution through super-oscillations *J. Opt. A: Pure Appl. Opt.* **9** S285
- [28] Huang F M, Kao T S, Fedotov V A, Chen Y and Zheludev N I 2008 Nanohole array as a lens *Nano Lett.* **8** 2469
- [29] Huang F M, Zheludev N I, Chen Y and Javier Garcia de Abajo F 2007 Focusing of light by a nanohole array *Appl. Phys. Lett.* **90** 091119



Copyright of New Journal of Physics is the property of IOP Publishing and its content may not be copied or emailed to multiple sites or posted to a listserv without the copyright holder's express written permission. However, users may print, download, or email articles for individual use.